Tuning Manganese Dopant Spin Interactions in Single GaN Nanowires at Room Temperature

Manu Hegde, Shokouh S. Farvid, Ian D. Hosein, and Pavle V. Radovanovic*

Department of Chemistry, University of Waterloo, 200 University Avenue West, Waterloo, Ontario N2L 3G1, Canada

ABSTRACT Control of electron spins in individual magnetically doped semiconductor nanostructures has considerable potential for quantum information processing and storage. The manipulations of dilute magnetic interactions have largely been restricted to low temperatures, limiting their potential technological applications. Among the systems predicted to be ferromagnetic above room temperature, Mn-doped GaN has attracted particular attention, due to its attractive optical and electrical properties. However, the experimental data have been inconsistent, and the origin of the magnetic interactions remains unclear. Furthermore, there has been no demonstration of tuning the dopant exchange interactions within a single nanostructure, which is necessary for the design of nanoscale spin-electronic (spintronic) devices. Here we directly show for the first time intrinsic magnetization of manganese dopants in individual gallium nitride nanowires (NWs) at room temperature. Using high-resolution circularly polarized X-ray microscopy imaging, we demonstrate the dependence of the manganese exchange interactions on the NW orientation with respect to the external magnetic field. The crystalline anisotropy allows for the control of dilute magnetization in a single NW and the application of bottom-up approaches, such as *in situ* nanowire growth control or targeted positioning of individual NWs, for the design of networks for quantum information technologies.

KEYWORDS: nanowires · diluted magnetic semiconductors · GaN · doping · anisotropy · magnetic ordering · X-ray absorption · XMCD · STXM

Simultaneous manipulation of spin and charge is the basis for spin-electronics (spintronics), which has been demonstrated as an attractive alternative to traditional charge-based electronics.[1,2] A promising approach to fabricating key elements for semiconductor spintronics is to substitutionally incorporate magnetic ions into semiconductors—the class of materials known as diluted magnetic semiconductors (DMSs).[3] The magnetic exchange interactions between unpaired electrons of transition metal dopants and the free carriers in the semiconductor host lattices (known as *sp-d* exchange interactions) could allow for both spin and charge of the carriers to be manipulated by an external magnetic field. These interactions have been extensively studied in Mn-doped GaAs (Mn:GaAs) as the model system.[4] Despite nearly 20 years of research into Mn:GaAs and continuing increase in the Curie temperature,[5] ferromagnetism in this material has been observed below 200 K,[6] which remains too low for technological applications. To be practically applicable for integrated spin-based quantum information processing, an ideal candidate DMS should exhibit spontaneous spin polarization at or above room temperature, have high charge carrier concentration and mobility, and preferably be transparent in the visible region.[1] The theoretical prediction[7] of Zener-type ferromagnetic interactions of manganese(II) ions doped in p-type GaN above room temperature has motivated numerous studies on Mn:GaN preparation and properties.[8−10] These studies have often arrived at different conclusions about the type and origin of the spin interactions, from ferromagnetism at room[8] or low temperature,[9] to mostly paramagnetic and antiferromagnetic behavior,[10] indicating a strong dependence of the magnetic properties on the synthesis method and conditions.

The bottom-up implementation of DMS-based spintronics technologies requires fabrication of nanostructures in which dilute spin interactions can be manipulated in a controlled fashion. Free-standing semiconductor nanowires (NWs) have been demonstrated to be a promising platform for a variety of nanodevices, from high-performance field-effect transistors for electronics[11] and bioprobes[12] to nanoscale lasers.[13] Quantitative investigation of the electronic structure of Mn dopants and their exchange interactions in individual GaN NWs is therefore critical to understanding the origin of the magnetic properties and manipulation of the spin states in DMS NWs. Oriented growth of NWs and the anisotropic crystal structure of wurtzite GaN (Figure 1) could enable the exploitation of the crystalline anisotropy for manipulating spin interactions in individual Mn:GaN NWs. Furthermore,

* Address correspondence to pavler@uwaterloo.ca.

Received for review April 22, 2011 and accepted July 15, 2011.

Published online July 22, 2011
10.1021/nn201482y

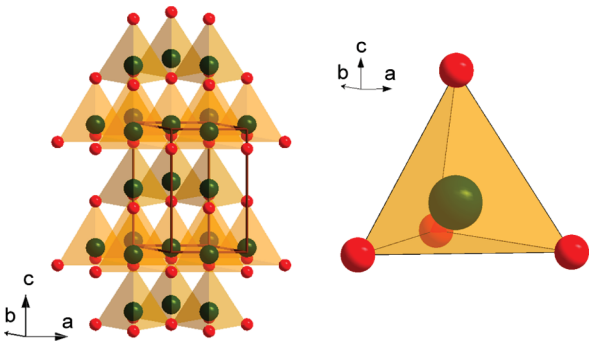

Figure 1. Crystal structure of wurtzite GaN showing a unit cell (left) and the coordination of a gallium ion site (right). Ga atoms are shown as green and N as red spheres. The orientation of the unit cell is shown with respect to the crystal coordinate system.

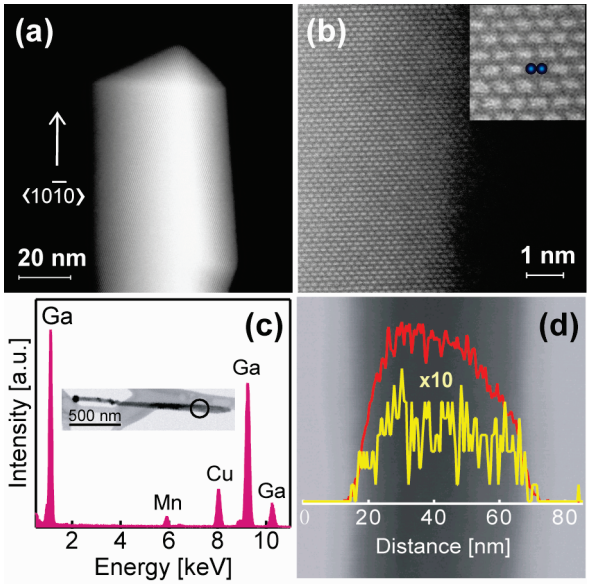

Figure 2. (a) STEM image of Mn:GaN nanowire showing triangular cross section. (b) HAADF-STEM image of Mn:GaN nanowire from part (a). Inset: magnified section of the image showing characteristic dumbbell structure consisting of pairs of Ga atoms separated by *ca.* 6 Å. The positions of Ga atoms are indicated with blue spheres. (c) EDX spectrum of a typical Mn:GaN nanowire. The nanowire region corresponding to the spectrum is designated with a circle in the inset. Mn doping concentration is determined to be 4.5 ± 0.3%. (d) EDX elemental line scan profile of the nanowire in (c), indicating very similar Mn (yellow) and Ga (red) profiles. The line profiles are overlapped on the nanowire image. Mn profile is multiplied by a factor of 10 for clarity.

faceting and growth direction of GaN NWs can be manipulated by the adsorption of Mn dopants on the NW surfaces during incorporation,[14,15] allowing for both spin polarization and anisotropy control. Despite significant interest in Mn:GaN NWs in recent years,[14−21] many of their properties are still not well understood. The information about Mn dopants has largely come from ensemble measurements, including X-ray photoelectron spectroscopy,[21] electron energy loss spectroscopy,[18] photoluminescence,[16] and X-ray absorption spectroscopy (XAS),[17,21] which detect all Mn species, including those co-deposited outside of the NWs during their growth by the chemical vapor deposition (CVD) method. Manipulation and measurements of dopant spin interactions within a single NW require a spin-sensitive dopant-specific nanometer-size probe with high spectral resolution. Such measurements could lead to the design of integrated NW-based architectures for quantum information processing. Here we demonstrate a precise control and measurement of the magnetic exchange interactions of Mn dopant ions within individual GaN NWs. Using circularly polarized scanning transmission X-ray microscopy (STXM) imaging, we show intrinsic room temperature magnetic ordering of $Mn^{2+/3+}$ ions substitutionally embedded into GaN NWs and demonstrate that the magnetization is strongly dependent on the orientation of the NWs relative to the external magnetic field. The dependence of the effective magnetic moment on the NW orientation is attributed to the crystalline anisotropy of wurtzite GaN lattice and could potentially be used to form networks for nanowire-based spintronic circuitry.

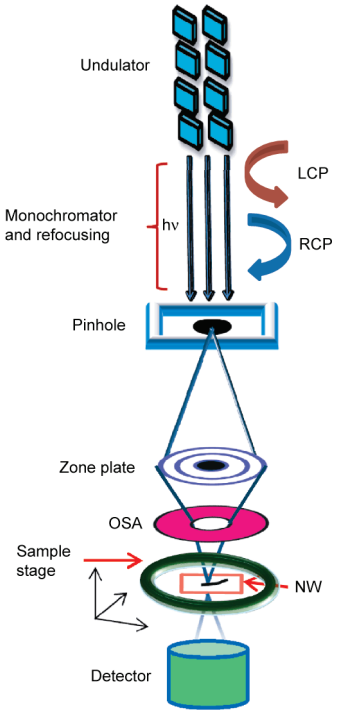

Figure 3. Schematic representation of STXM. X-rays from the synchrotron source are passed through the pinhole. The Fresnel zone plate focuses the X-ray beam through order sorting aperture (OSA) in the sample plane. The specimen is raster-scanned in the focal plane of X-rays, and the transmitted photons are recorded by an X-ray-sensitive detector generating an image of the specimen. For XMCD measurements, the beam polarization (>95%) is achieved by the choice of a proper undulator.

RESULTS AND DISCUSSION

Atomic-Level Structure of Mn Dopants in GaN Nanowires. Manganese-doped GaN NWs were synthesized by chemical vapor deposition (CVD), using Mn starting concentration of *ca.* 10 atom % ([Mn]/[Ga] ≈ 0.10). Most of these NWs had triangular cross section and grew along the $\langle 10\bar{1}0 \rangle$ direction, as previously reported for the samples synthesized with similar starting concentration of Mn precursor (Figure 2a and Figure S1 in Supporting Information).[15] Figure 2b shows high-angle annular dark-field (HAADF) scanning transmission electron microscopy (STEM) image of Mn:GaN NW from Figure 2a. This technique is sensitive to changes in the atomic number (*Z*) within the specimen and is often referred to as *Z*-contrast imaging. Due to a signficantly higher *Z* value of Ga with respect to N, only Ga sites are directly observed. Horizontally elongated spots in the image correspond to two Ga^{3+} sites separated by *ca.* 6 Å (Figure 2b, inset). This dumbbell structure characteristic for wurtzite GaN remains intact upon Mn ion incorporation. Careful inspection of different NWs with this resolution and atomic weight specificity rules out the presence of secondary phases of Mn dopants, even in very small domains, within individual NWs. The average doping concentration was determined by energy-dispersive X-ray (EDX) spectroscopy to be 4.5 ± 0.3 atom %

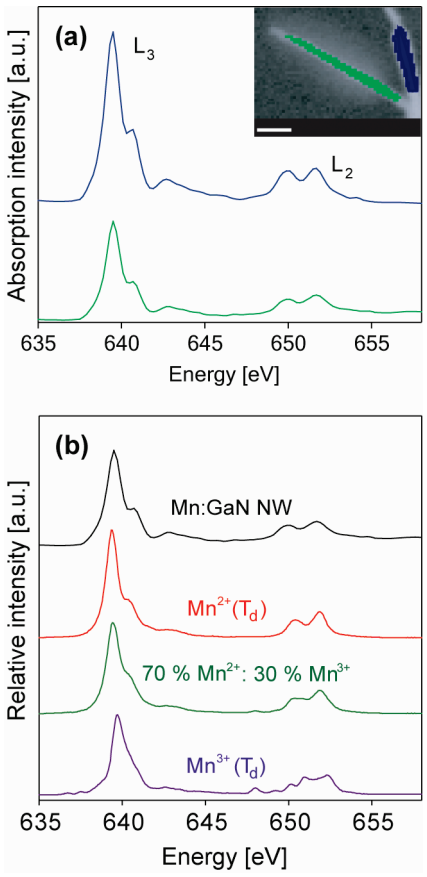

Figure 4. (a) Mn $L_{2,3}$-edge X-ray absorption spectra of single Mn:GaN NWs obtained by STXM at 300 K. The image in the inset, taken with 633.0 eV photons, shows the area of the specimen from which the spectra were extracted (scale bar, 0.5 μm). The spectra correspond to the NW regions designated with the analogous colors in the image. (b) Mn $L_{2,3}$-edge single NW absorption spectrum (black) compared to the theoretical spectra of Mn^{2+} (red) and Mn^{3+} (purple) in tetrahedral coordination calculated by CI cluster-model method (taken from ref 26). Linear combination analysis suggests the experimental spectrum is well matched to the theoretical spectrum for the dopant composition of 70% Mn^{2+} and 30% Mn^{3+} (green).

(Figure 2c). EDX elemental line scan profile of the same NW recorded perpendicular to the growth direction is shown in Figure 2d. The line scan profile of Mn is in good agreement with that of Ga, indicating largely random distribution of Mn across the NW.[15] Although Mn:GaN NWs obtained by the CVD method under the given conditions can practically be considered homogeneously doped, we note that, at some places along the NW, Mn profile may be slightly lower in the middle of the NW relative to Ga. This is occasionally observed close to the NW tips and is associated with the doping mechanism involving binding of Mn intermediates to the NW surfaces (vapor–solid rather than vapor–liquid–solid doping mechanism).[15,22]

To understand the electronic structure and oxidation state of Mn dopant ions in individual NWs, we employed STXM (Figure 3). In these experiments, a monoenergetic X-ray beam (*ca.* 30 nm in diameter)

provided by a third-generation synchrotron source is focused on a particular area of the sample, and an image is generated by monitoring the transmitted X-ray signal as the specimen is raster-scanned at the focus of the X-rays (Supporting Information movie). Figure 4a (inset) shows a STXM image of typical NWs, collected using 633 eV X-ray beam. The absorption spectrum of a particular sample area at a given element edge is reconstructed from the stack of images by monitoring the transmitted intensities for different photon energies. Mn $L_{2,3}$-edge spectra corresponding to the selected NW areas are shown with analogous colors in Figure 4a. The structured asymmetric peak centered at approximately 640 eV can be assigned to L_3-edge (predominantly p→d in character) and the lower intensity feature centered at ~651 eV to L_2-edge absorption. Both spectra are very similar, indicating high wire-to-wire uniformity in Mn ion speciation (also Figure S2, Supporting Information). Theoretical modeling of the Mn K-edge X-ray absorption spectra has suggested that the substitutional model with Mn dopants on Ga^{3+} sites best simulates the experimental data.[23] This finding is consistent with the extensive density functional theory calculations,[24] which have predicted that the formation energy of the substitutional Mn in GaN is significantly smaller (by *ca.* 5−7 eV) than the formation energies of interstitial octahedral or tetrahedral Mn species. Furthermore, the L-edge spectra corresponding to interstitial Mn in GaN are expected to be significantly different from substitutional (simple or neighboring N split interstitial) sites.[25] We therefore considered substitutional sites as the most likely form of Mn incorporation. To further understand the nature of the doping sites and the Mn oxidation state, we analyzed the data with respect to the theoretical spectra for Mn^{2+} and Mn^{3+} in tetrahedral (T_d) coordination calculated by configuration−interaction (CI) cluster-model method.[26] The red and purple traces in Figure 4b represent the $L_{2,3}$-edge spectra of tetrahedral Mn^{2+} and Mn^{3+}, respectively. While the general features of these two spectra are similar, there is a significant structural difference, particularly in the L_2 region, which has a multiplet structure for Mn^{3+}.[26] The similarity between the Mn $L_{2,3}$-edge spectra of single Mn:GaN NWs and the simulated spectra indicates that Mn ions are present in T_d coordination in GaN NWs. Careful examination of the experimental data (Figure 4b, black trace) indicates that both Mn^{2+} and Mn^{3+} contribute to the observed spectrum, although Mn^{2+} is the dominant form. To analyze more quantitatively the oxidation states of Mn in single Mn:GaN NWs, we performed linear combination analysis using the calculated spectra of Mn^{2+} and Mn^{3+}. The best fit of the experimental data is obtained for approximately 70% Mn^{2+} and 30% Mn^{3+} (Figure 4b, green trace).

Magnetic Properties of a Single Mn-Doped GaN Nanowire. Magnetization properties of single Mn:GaN NWs arising from Mn dopant ion interactions were studied by X-ray magnetic circular dichroism (XMCD) imaging using STXM. XMCD measures the difference in absorption of left circularly polarized (LCP, ρ^-) and right circularly polarized (RCP, ρ^+) X-ray beams in external magnetic field and provides for highly specific detection of exchange interactions of Mn dopant ions in individual NWs. For XMCD measurements, the NWs were deposited on a TEM grid which was mounted between small device-size magnetic poles (Figure 5a) and tilted in the beam path (*ca.* 30° from normal incidence) to allow for a parallel component of the magnetic field relative to the X-ray propagation direction (Figure 5b). The selected NWs were imaged alternately with ρ^+ and ρ^- X-rays at different photon energies, allowing for an extraction of XMCD spectra with nanometer scale spatial resolution. An imbalance of the spin-up and spin-down states in partially populated d orbitals, associated with the net magnetic moment, can be effectively probed by the excitation of 2p core electrons to unfilled 3d states (d holes) by ρ^+ and ρ^- photons (Figure 5c). The angular momenta of the photons with the opposite helicity are coupled with the excited photoelectrons and subsequently transferred to spins through spin−orbit coupling.[2,27] The sign of dichroic signal is opposite for L_3- and L_2-edges because they have opposite spin−orbit coupling (l−s and l+s for L_2 and L_3, respectively). Figure 5d shows the absorption spectra for ρ^+ and ρ^- and the corresponding XMCD spectrum of a typical NW in the region parallel to the magnetic field direction (orange area in the inset of Figure 5d). The observed XMCD spectrum attests to the room temperature magnetization arising from substitutional Mn dopant ions in the nanowire. The determination of the spin ($m_S = -2\langle S_z\rangle\mu_B/\hbar$) and orbital magnetic moment ($m_L = -\langle L_z\rangle\mu_B/\hbar$) contributions to the total effective magnetic moment in the units of μ_B/atom is possible by the use of sum rules,[28] neglecting the expectation value of the magnetic dipole operator $\langle T_z\rangle$:

$$m_L = -\frac{4}{3}N_h\frac{\int(\Delta\rho_{L3}+\Delta\rho_{L2})dE}{\int_{L_3+L_2}(\rho^+ + \rho^-)dE}$$
$$m_S = -2N_h\frac{\int(\Delta\rho_{L3}-2\Delta\rho_{L2})dE}{\int_{L_3+L_2}(\rho^+ + \rho^-)dE} + 7\langle Tz\rangle \quad (1)$$

where $\Delta\rho_{L_2}$ and $\Delta\rho_{L_3}$ are the XMCD signals ($\rho^- - \rho^+$) at the L_2- and L_3-edges, respectively, N_h is the number of d holes, and the denominators are the total integrated sum spectra for ρ^+ and ρ^-. On the basis of the ratio of Mn ions with +2 and +3 oxidation states, we used a N_h value of 5.3 for this calculation. This analysis allows for the quantitative determination of the effective magnetic moment contributions such that $m_S = 0.27\,\mu_B$/Mn and $m_L = -0.03\,\mu_B$/Mn. A relatively large contribution

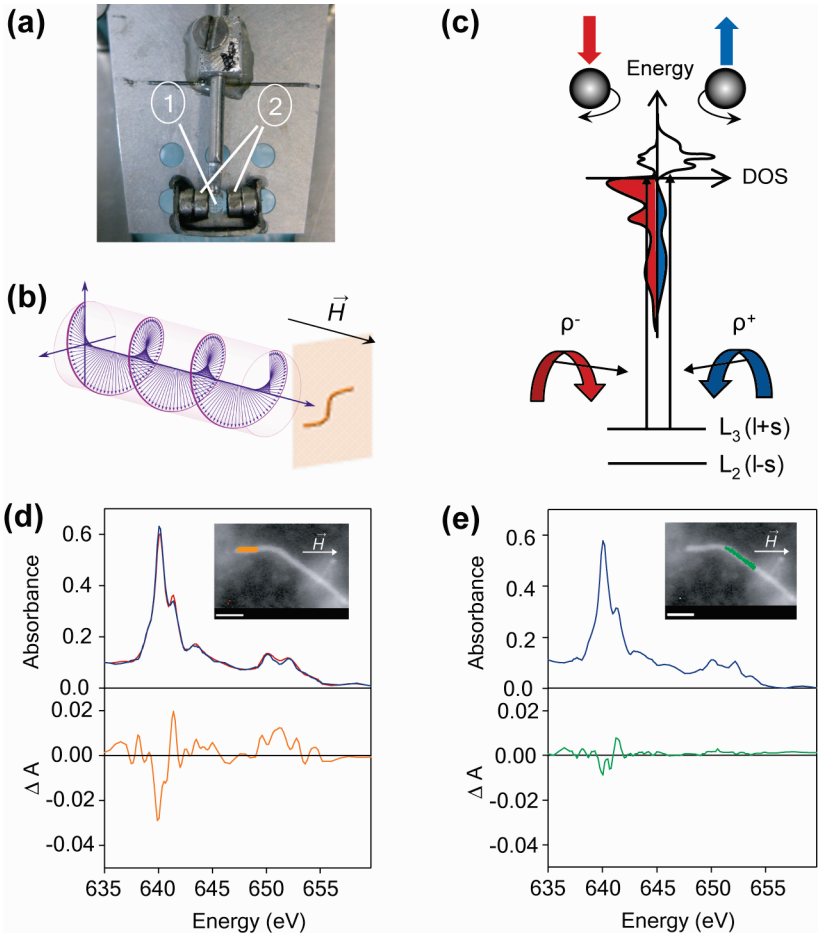

Figure 5. (a) Photograph of the experimental setup for XMCD measurements by STXM. A fraction of a TEM grid with deposited nanowires (1) is placed between the poles of the device-size magnet (2). (b) Configuration of XMCD microscopy measurements. The setup shown in (a) is placed in the beam path *ca.* 30° with respect to the normal incidence, which allows a component of the applied magnetic field (<0.1 T) to be oriented parallel to the propagation of the circularly polarized photons. The spectra were obtained by alternate imaging with LCP and RCP photons. (c) Schematic representation of the density of states (DOS) of Mn in GaN nanowires indicating the spin orientations (blue and red arrows). The XMCD transitions occur from the spin−orbit split 2p shell to empty 3d states of Mn dopants (black arrows). (d,e) Mn $L_{2,3}$-edge XMCD spectra collected at 300 K of a nanowire in the region parallel (d) and making 37° angle (e) with the magnetic field direction, obtained as a difference between ρ^- (red) and ρ^+ (blue). The nanowire regions corresponding to XMCD spectra are shown in the insets (scale bars, 0.8 μm).

of m_L (*ca.* 10%) having the opposite sign of m_S indicates a significant spin−orbit interaction in GaN NWs, and that m_S and m_L are coupled antiparallel. The determined net magnetic moment is estimated to be at least an order of magnitude larger than the magnetization of paramagnetic Mn:GaN crystals,[10] suggesting a long-range ordering of Mn dopants in GaN NWs. It should be emphasized that this magnetization is detected at subsaturation effective magnetic field strength (<0.1 T). Therefore, it is notable that this dilute intrinsic magnetic ordering can be observed and quantitatively determined at room temperature in individual NWs using a miniature device-size magnet. Although these data indicate intrinsic ferromagnetism arising from Mn dopants, the mechanism of magnetic ordering may still be open to debate.[25,29,30] The substitution of Mn^{2+} for Ga^{3+} leads to hole formation in GaN NWs, which can mediate magnetic ordering, although possibly by a mechanism[30] different from that initially proposed by Dietl *et al.*[7] The defects[25] and surfaces[29] may also have a significant impact on ferromagnetic interactions in one-dimensional DMSs. Unlike the XMCD spectrum of the NW section oriented parallel to the direction of the magnetic field, the spectrum of the NW area oriented 37° with respect to the magnetic field direction (Figure 5e) shows much lower intensity of the magnetic moment for nearly identical average absorption intensity.

Anisotropy-Tunable Spin-Exchange Interactions in Mn-Doped GaN Nanowire Assembly. The dependence of the spin magnetic moment on the NW orientation suggests anisotropy effect on the magnetic exchange interactions. For dilute magnetization, it is unlikely that the orientation dependence comes from the shape anisotropy.[31] Instead, we hypothesized that crystalline anisotropy is responsible for the observed difference in magnetization for the

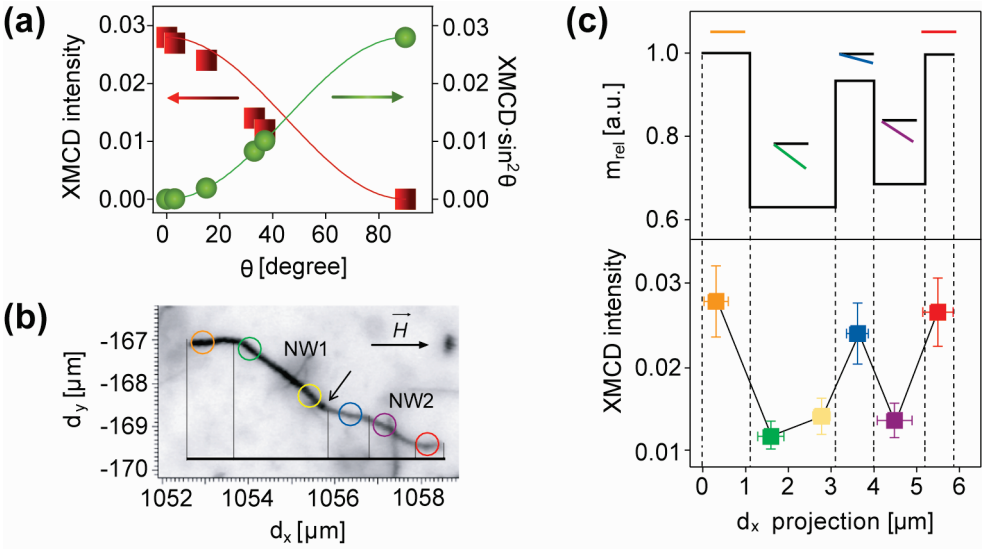

Figure 6. Orientation-tunable spin interactions in single Mn:GaN NWs. (a) XMCD intensity measured at 640 eV (at 300 K) *vs* angle θ between the nanowire long axis and the magnetic field direction (red squares). This relation is opposite from XMCD·sin^2 θ dependence on θ (green spheres), indicating crystalline anisotropy origin of the change in XMCD intensity with nanowire orientation. Red and green lines are simulated cos^2 θ and sin^2 θ dependences, respectively. (b) STXM image (at 633 eV) of two joined nanowires (the point of junction is indicated by the black arrow). The circled areas indicate the regions on the nanowires probed by XMCD. The direction of the magnetic field is parallel to d_x. (c) Simulated relative change in magnetic moment based on the change in crystalline anisotropy energy along d_x (upper part). The colored lines above the graph indicate the NW orientation with respect to the magnetic field direction (black lines). Measured XMCD intensities in the regions circled in part (b) are shown with analogous colors in the lower part as a function of d_x. Error bars indicate standard uncertainty in XMCD measurements (y-axis) and d_x range for the NW regions from which XMCD was extracted (x-axis).

two investigated areas of the NW. To establish the origin of the dependence of Mn exchange interactions on the NW orientation, we plotted the maximum L_3-edge XMCD intensities, corresponding to the equivalent average absorption spectra, as a function of the angle θ between the NW orientation and the magnetic field direction (Figure 6a, red squares). The effective magnetic moment of Mn decreases with increasing θ, becoming nondetectable for $\theta = 90°$. Spontaneous magnetization in different crystallographic directions is characterized by the magnetocrystalline anisotropy energy (E_{an}), which has the minimum value for the easy axis of magnetization.[31] The anisotropy energy for uniaxial crystals is described by a series expansion, which can be reduced to

$$E_{an} = K_0 + K_1 \sin^2 \theta \qquad (2)$$

where K_0 and K_1 are anisotropy constants. Calculations of the anisotropy energy have shown that the Mn magnetic moment is oriented preferentially along the $\langle 10\bar{1}0 \rangle$ direction in GaN,[29] which is the dominant NW growth direction in this study. The results of this work are therefore in agreement with the theoretical predictions.[29] Other contributions to magnetic anisotropy include the anisotropy of the local potential experienced by the bound hole[32] or possibly the contribution arising from Mn^{3+}. The difference in energy of magnetization per unit volume of material for magnetic moments parallel and perpendicular to the easy axis is $E_\perp - E_\parallel = K_1$. Therefore, E_{an} should be

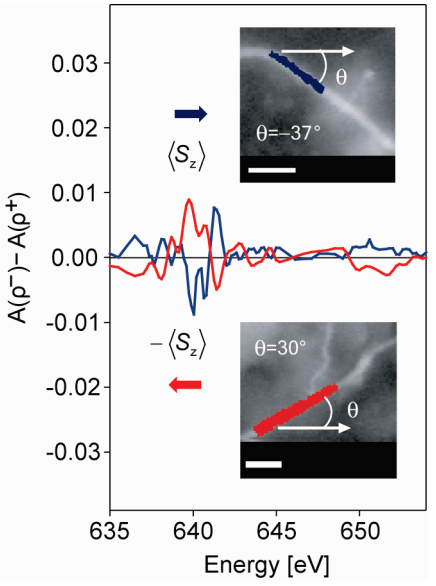

Figure 7. XMCD spectra (300 K) of two NWs (shown in the insets) having the opposite orientation with respect to the magnetic field. The change in the sign of XMCD for two NW orientations attests to the reversal in spin orientation. Scale bars, 0.8 μm.

inversely correlated with magnetization and increase symmetrically to a decrease in XMCD intensity, obeying sin^2 θ dependence (Figure 6a, green spheres). Conversely, XMCD intensity itself follows cos^2 θ dependence (Figure 6a, red line). The measured variation of XMCD intensity attests to the magnetocrystalline

anisotropy as the origin of the magnetization dependence on the NW orientation. These results demonstrate tunability of dilute spin-exchange interactions in DMS NWs at room temperature through NW orientation. This orientation dependence was confirmed by the analysis of at least 10 different NWs that we were able to investigate during the given experimental time, demonstrating the reproducibility of the effect within the sample.

The orientation dependence can, in principle, be exploited to design nanowire-based network structures that could be used for quantum information processing. One such example, shown in Figure 6b, is a simple motif of alternate NW orientations, which can be formed by selecting the NWs based either on their longitudinal morphology or simple van der Waals bonding of different NWs. Both examples are demonstrated in Figure 6b, in which two bent NWs are joined together forming a recurring motif. The expected XMCD intensity for the magnetic field direction shown in Figure 6b should change with the NW orientation according to $\cos^2 \theta$ dependence. The simulated relative change in magnetic moment as a function of the NW projection distance along the magnetic field direction (d_x) is shown in Figure 6c (upper part). Experimentally measured Mn L_3-edge XMCD maxima corresponding to normalized absorption spectra recorded along the NW assembly show very good agreement with the predicted magnetization behavior (Figure 6c, colored squares), demonstrating the potential to reproducibly tune the magnitude of Mn dopant exchange interactions by NW orientation.

An important aspect of exploiting NW orientation for controlling spin-exchange interactions of magnetic dopants is the possibility of the reversal of spin polarization. Figure 7 shows XMCD spectra of two NWs (shown in the insets) making an angle of *ca.* 30° with the magnetic field direction, but in the opposite directions—one clockwise the other one counterclockwise. The opposite NW orientation is equivalent to different handedness, which can also be achieved by switching the poles of the magnetic field, or rotating the specimen 180° around the vertical axis. This difference in the rotational direction results in reversal of the signs of XMCD peaks, indicating opposite spin orientation for two different NW configurations. On the basis of the orientation-dependent magnetization of NWs demonstrated in this work, it is expected that the magnetic susceptibility of as-synthesized NW samples measured by an ensemble method should be negligible. This hypothesis was confirmed by measuring the magnetic hysteresis loop of the NWs on the growth substrate (Figure S3, Supporting Information), which shows only very small residual net magnetic moment. The comparison with ensemble measurements underscores the importance of single NW magnetization studies for truly understanding the magnetic properties of DMS NW systems. The ability to tune the magnitude and sign of the spin-exchange interactions in single NWs at room temperature using small device-size magnetic fields demonstrates the feasibility of nanowire-based spintronic circuits and opens the door for building networks for scalable quantum information processing by assembling individual NW elements.

CONCLUSION

Using XAS and XMCD measurements in STXM configuration, we quantified the electronic structure and intrinsic spin and orbital magnetic moments of Mn dopants in a single GaN nanowire at room temperature. This work demonstrates strong anisotropy dependence of dilute magnetization in GaN nanowires and allows for a control of the dopant exchange interactions within single nanowires or in nanowire assembly, based on their growth and positioning. Manipulation of dilute magnetization in individual semiconductor nanowires at room temperature offers unprecedented opportunities for future spintronics and quantum information processing technologies. These results inspire future studies of doped nanowires at even higher spectral and spatial resolution, which may reveal new possibilities for spin manipulation in semiconductor nanostructures[33] and improve the microscopic understanding of dilute magnetic ordering in nanoscale semiconductors. With the development and optimization of nanowire growth and assembly techniques, including Langmuir–Blodgett technique[34] and superlattice nanowire pattern transfer,[35] the potential for fabrication of practical nanowire spintronic devices could become a reality.

METHODS

Synthesis of Mn-Doped GaN Nanowires. Mn-doped GaN nanowires were synthesized by the chemical vapor deposition (CVD) method.[14,15] The synthesis was performed from Ga metal ingots (99.99%, Strem Chemicals) and anhydrous $MnCl_2$ (97%, Alfa Aesar) under the flow of gaseous ammonia (50 sccm, high purity, grade 5.5) and hydrogen (100 sccm, high purity, grade 5). The nanowires were grown in a 2 in. three-zone tube furnace at 950 °C on a sapphire substrate, which was placed about 1 cm downstream of the solid precursor mixture. Nickel nanoparticles, prepared *in situ* from $Ni(NO_3)_2$ deposited on the growth substrate from an ethanol solution, were used as catalysts. The reaction was allowed to proceed for 20 min at the pressure of 200 Torr, at which point the gas flow was stopped, and the reaction products were allowed to cool slowly under an argon flow.

Characterization. The samples were characterized with X-ray diffractometer (XRD, INEL), scanning electron microscope (SEM, LEO 1530), and high-resolution transmission electron microscope (HRTEM, JEOL 2010F). *Z*-contrast scanning transmission electron microscopy (STEM) experiments were performed with FEI Titan 80-300 cubed electron microscope at the Canadian Centre for Electron Microscopy at McMaster University. The microscope is equipped with a hexapole-based aberration corrector for the image forming lens (which forms the high

annular dark-field image) and a corrector for the probe forming lens. The instrument can achieve subangstrom resolution for phase contrast imaging and STEM.

STXM Imaging. Scanning transmission X-ray microscopy (STXM) experiments were carried out at Soft X-ray Spectro-Microscopy (SM) beamline (10ID-1) the Canadian Light Source, which is capable of generating soft X-rays in the range of 130−2500 eV. A polarized X-ray beam was obtained using a 2 m long, 76 mm period Apple II undulator. The X-ray beam was passed through a pinhole aperture and focused on the sample plane using Fresnel zone plate (ZP). The beam from the ZP passed through a molybdenum-based order sorting aperture (OSA), with a 50 μm pinhole. The OSA allowed only first-order ZP diffracted light to pass. An image was generated by capturing the transmitted X-ray signal from a region of interest. The scheme of STXM experimental setup is shown in Figure 3.

XAS and XMCD Measurements and Data Analysis. For XAS measurements, the NWs were deposited on a silicon nitride substrate from a dilute suspension in ethanol. Image stacks were collected for different energies from 633.0 to 660.0 eV (Mn $L_{2,3}$-edge) at room temperature (*ca.* 300 K). The analysis of the X-ray microscopy images and spectra was performed using Axis 2000 software. The collected image stacks were aligned using Jacobson Analysis software. A given image stack for a particular set of energies contains the intensity of the transmitted X-rays, which was converted into optical density (OD) values using the relation $\ln(I/I_0)$, where I is the signal transmitted through a desired sample area and I_0 is the signal from the image area with no sample. For XMCD measurements, NWs were deposited on a TEM grid, which was sliced under an optical microscope in three parts of nearly equal width. The middle section was fixed on a nonmagnetic rod using epoxy and placed between the poles of a small permanent magnet (Figure 5a). This setup was inserted into the beam path so that the X-ray beam direction makes a ~30° angle with the specimen normal. This angle allows for a magnetic field axis to be parallel to the beam propagation direction (necessary for a dichroism effect) as well as an unobstructed beam path and sufficient specimen projection for convenient data collection. Circularly polarized light was obtained by choosing a proper undulator. The selected specimen area was imaged at each energy alternately with the opposite photon helicity (ρ^+ and ρ^-) to eliminate any possible inconsistencies over time. Room temperature XMCD measurements were carried out at the Mn $L_{2,3}$-edge. The absorption spectra for ρ^+ and ρ^- were obtained in the same way as for XAS. The determination of the spin (m_S) and orbital magnetic moment (m_L) contributions to the total effective magnetic moment in the units of μ_B/atom is possible by the use of sum rules (eqs 1), as described in the text. The expectation value of the magnetic dipole operator $\langle T_z \rangle$ is readily neglected.[28] The orbital momentum branching ratio is influenced by spin−orbit interaction-based imbalance between $d_{3/2}$ and $d_{5/2}$ final states.[36] Due to the resulting nonvanishing strong orbital momentum, no spin-correction factor was applied.

Acknowledgment. This work was supported by the NSERC (Discovery Grant, ID 341919), CFI and CRC program (P.V.R.). S.S.F. acknowledges Waterloo Institute for Nanotechnology (WIN) for a partial support through the Graduate Research Fellowship. S.S.F. and M.H. thank Canadian Light Source (CLS) for Graduate Travel Support awards. The research described was partly performed at the CLS, which is supported by the NSERC, NRC, CIHR, the Province of Saskatchewan, Western Economic Diversification Canada, and the University of Saskatchewan. We thank Dr. Jian Wang for his assistance at 10ID-1 beamline. Electron microscopy work was performed at the Canadian Centre for Electron Microscopy at McMaster University.

Supporting Information Available: TEM image of Mn:GaN NW, additional Mn $L_{2,3}$-edge X-ray absorption spectra of single Mn:GaN NWs, magnetic susceptibility measurements of as-grown Mn:GaN NWs, a movie showing the STXM images from which the absorption spectra were extracted. This material is available free of charge *via* the Internet at http://pubs.acs.org.

REFERENCES AND NOTES

1. Wolf, S. A.; Awschalom, D. D.; Buhrman, R. A.; Daughton, J. M.; von Molnar, S.; Roukes, M. L.; Chtchelkanova, A. Y.; Treger, D. M. Spintronics: A Spin-Based Electronics Vision for the Future. *Science* **2001**, *294*, 1488–1495.
2. Zutic, I.; Fabian, J.; Das Sarma, S. Spintronics: Fundamentals and Applications. *Rev. Mod. Phys.* **2004**, *76*, 323–410.
3. Furdyna, J. K.; Kossut, J. Diluted Magnetic Semiconductors. In *Semiconductors and Semimetals*; Willardson, R. K., Beer, A. C., Eds.; Academic Press: New York, 1988; Vol. 25.
4. Ohno, H. Making Nonmagnetic Semiconductors Ferromagnetic. *Science* **1998**, *281*, 951–956.
5. Ku, K. C.; Potashnik, S. J.; Wang, R. F.; Chun, S. H.; Schiffer, P.; Samarth, N.; Seong, M. J.; Mascarenhas, A.; Johnston-Halperin, E.; Myers, R. C.; *et al.* Highly Enhanced Curie Temperature in Low-Temperature Annealed [Ga,Mn]As Epilayers. *Appl. Phys. Lett.* **2003**, *82*, 2302–2304.
6. Novak, V.; Olejnik, K.; Wunderlich, J.; Cukr, M.; Vyborny, K.; Rushforth, A. W.; Edmonds, K. W.; Campion, R. P.; Gallagher, B. L.; Sinova, J.; *et al.* Curie Point Singularity in the Temperature Derivative of Resistivity in (Ga,Mn)As. *Phys. Rev. Lett.* **2008**, *101*, 077201.
7. Dietl, T.; Ohno, H.; Matsukura, F.; Cibert, J.; Ferrand, D. Zener Model Description of Ferromagnetism in Zinc-Blende Magnetic Semiconductors. *Science* **2000**, *287*, 1019–1022.
8. Sonoda, S.; Shimizu, S.; Sasaki, T.; Yamamoto, Y.; Hori, H. Molecular Beam Epitaxy of Wurtzite (Ga,Mn)N Films on Sapphire (0001) Showing the Ferromagnetic Behaviour at Room Temperature. *J. Cryst. Growth* **2002**, *237−239*, 1358–1362.
9. Sarigiannidou, E.; Wilhelm, F.; Monroy, E.; Galera, R. M.; Bellet-Amalric, E.; Rogalev, A.; Goulon, J.; Cibert, J.; Mariette, H. Intrinsic Ferromagnetism in Wurtzite (Ga,Mn-)N Semiconductor. *Phys. Rev. B* **2006**, *74*, 041306(R).
10. Zajac, M.; Gosk, J.; Kaminska, M.; Twardowski, A.; Szyszko, T.; Podsiadlo, S. Paramagnetism and Antiferromagnetic d−d Coupling in GaMnN Magnetic Semiconductor. *Appl. Phys. Lett.* **2001**, *79*, 2432–2434.
11. Cui, Y.; Zhong, Z.; Wang, D.; Wang, W. U.; Lieber, C. M. High Performance Silicon Nanowire Field Effect Transistors. *Nano Lett.* **2003**, *3*, 149–152.
12. Tian, B.; Cohen-Karni, T.; Qing, Q.; Duan, X.; Xie, P.; Lieber, C. M. Three-Dimensional, Flexible Nanoscale Field-Effect Transistors as Localized Bioprobes. *Science* **2010**, *329*, 831–834.
13. Duan, X.; Huang, Y.; Agarwal, R.; Lieber, C. M. Single-Nanowire Electrically Driven Lasers. *Nature* **2003**, *421*, 241–245.
14. Stamplecoskie, K. G.; Ju, L.; Farvid, S. S.; Radovanovic, P. V. General Control of Transition-Metal-Doped GaN Nanowire Growth: Toward Understanding the Mechanism of Dopant Incorporation. *Nano Lett.* **2008**, *8*, 2674–2681.
15. Radovanovic, P. V.; Stamplecoskie, K. G.; Pautler, B. G. Dopant Ion Concentration Dependence of Growth and Faceting of Manganese-Doped GaN Nanowires. *J. Am. Chem. Soc.* **2007**, *129*, 10980–10981.
16. Deepak, F. L.; Vanitha, P. V.; Govindaraj, A.; Rao, C. N. R. Photoluminescence Spectra and Ferromagnetic Properties of GaMnN Nanowires. *Chem. Phys. Lett.* **2003**, *374*, 314–318.
17. Seong, H.-K.; Kim, U.; Kim, M.-H.; Lee, H.-H.; Lee, D.-R.; Kim, J.-Y.; Choi, H.-J. Structural and Chemical Characterization of Mn Doped GaN Nanowires by X-ray Absorption Spectroscopy. *J. Nanosci. Nanotechnol.* **2009**, *9*, 6772–6776.
18. Choi, H.-J.; Seong, H.-K.; Chang, J.; Lee, K.-I.; Park, Y.-J.; Kim, J.-J.; Lee, S.-K.; He, R.; Kuykendall, T.; Yang, P. Single-Crystalline Diluted Magnetic Semiconductor GaN:Mn Nanowires. *Adv. Mater.* **2005**, *17*, 1351–1356.
19. Xu, C.; Chun, J.; Lee, H. J.; Jeong, Y. H.; Han, S.-E.; Kim, J.-J.; Kim, D. E. Ferromagnetic and Electrical Characteristics of *In Situ* Manganese-Doped GaN Nanowires. *J. Phys. Chem. C* **2007**, *111*, 1180–1185.
20. Han, D. S.; Park, J.; Rhie, K. W.; Kim, S.; Chang, J. Ferromagnetic Mn-Doped GaN Nanowires. *Appl. Phys. Lett.* **2005**, *86*, 032506.

21. Hwang, S. O.; Kim, H. S.; Park, S.-H.; Park, J.; Bae, S. Y.; Kim, B.; Park, J. Y.; Lee, G. Selective Growth of Straight and Zigzagged $Ga_{1-x}Mn_xN$ ($0 \leq x \leq 0.05$) Nanowires and Dependence of Their Electronic Structure and Magnetization on the Mn Content. *J Phys. Chem. C* **2008**, *112*, 2934–2942.
22. Perea, D. E.; Hemesath, E. R.; Schwalbach, E. J.; Lensch-Falk, J. L.; Voorhees, P. W.; Lauhon, L. J. Direct Measurement of Dopant Distribution in an Individual Vapour–Liquid–Solid Nanowire. *Nat. Nanotechnol.* **2009**, *4*, 315–319.
23. Bacewicz, R.; Filipowicz, J.; Podsiadlo, S.; Szyszko, T.; Kaminski, M. Probing Local Order in (Ga,Mn)N Alloys by X-ray Absorption Spectroscopy. *J. Phys. Chem. Solids* **2003**, *64*, 1469–1472.
24. Cui, X. Y.; Delley, B.; Freeman, A. J.; Stampfl, C. Neutral and Charged Embedded Clusters of Mn in Doped GaN from First Principles. *Phys. Rev. B* **2007**, *76*, 045201.
25. Keavney, D. J.; Cheung, S. H.; King, S. T.; Weinert, M.; Li, L. Role of Defect Sites and Ga Polarization in the Magnetism of Mn-Doped GaN. *Phys. Rev. Lett.* **2005**, *95*, 257201.
26. Hwang, J. I.; Kobayashi, M.; Song, G. S.; Fujimori, A.; Tanaka, A.; Yang, Z. S.; Lin, H. J.; Huang, D. J.; Chen, C. T. X-ray Magnetic Circular Dichroism Characterization of GaN/$Ga_{1-x}Mn_xN$ Digital Ferromagnetic Heterostructure. *Appl. Phys. Lett.* **2007**, *91*, 072507.
27. Stohr, J. Exploring the Microscopic Origin of Magnetic Anisotropies with X-ray Magnetic Circular Dichroism (XMCD) Spectroscopy. *J. Magn. Magn. Mater.* **1999**, *200*, 470–497.
28. Chen, C. T.; Idzerda, Y. U.; Lin, H.-J.; Smith, N. V.; Meigs, G.; Chaban, E.; Ho, G. H.; Pellegrin, E.; Sette, F. Experimental Confirmation of the X-ray Magnetic Circular Dichroism Sum Rules for Iron and Cobalt. *Phys. Rev. Lett.* **1995**, *75*, 152–155.
29. Wang, Q.; Sun, Q.; Jena, P. Ferromagnetism in Mn-Doped GaN Nanowires. *Phys. Rev. Lett.* **2005**, *95*, 167202.
30. Feng, Y.; Badaeva, E.; Gamelin, D. R.; Li, X. Excited-State Double Exchange in Manganese-Doped ZnO Quantum Dots: A Time-Dependent Density-Functional Study. *J. Phys. Chem. Lett.* **2010**, *1*, 1927–1931.
31. McCurrie, R. A. *Ferromagnetic Materials Structure and Properties*; Academic Press: London, 1994.
32. Krebs, O.; Benjamin, E.; Lemaitre, A. Magnetic Anisotropy of Singly Mn-Doped InAs/GaAs Quantum Dots. *Phys. Rev. B* **2009**, *80*, 165315.
33. Oszwaldowski, R.; Zutic, I.; Petukhov, A. G. Magnetism in Closed-Shell Quantum Dots: Emergence of Magnetic Bipolarons. *Phys. Rev. Lett.* **2011**, *106*, 177201.
34. Whang, D.; Jin, S.; Wu, Y.; Lieber, C. M. Large-Scale Hierarchical Organization of Nanowire Arrays for Integrated Nanosystems. *Nano Lett.* **2003**, *3*, 1255–1259.
35. Melosh, N. A.; Boukai, A.; Diana, F.; Gerardot, B.; Badolato, A.; Petroff, P. M.; Heath, J. R. Ultrahigh-Density Nanowire Lattices and Circuits. *Science* **2003**, *300*, 112–115.
36. Goering, E. X-ray Magnetic Circular Dichroism Sum Rule Correcition for the Light Transition Metals. *Philos. Mag.* **2005**, *85*, 2895–2911.